



Cite this: *Chem. Commun.*, 2024, 60, 14924

# A review on solid–solid heterogeneous interfacial interactions in electrocatalytic conversion of inorganic molecules

Wen-Xuan Liang,<sup>†,ab</sup> Huimin Han,<sup>†,ac</sup> Chun-Hua Zhen,<sup>b</sup> Yingjie Hua,<sup>c</sup> Jun-Tao Li<sup>id</sup><sup>a</sup> and Yao Zhou<sup>id</sup><sup>\*a</sup>

In electro-catalytical conversion of inorganic molecules, solid–solid interfaces universally form during the synthesis of electrocatalysts and the preparation of electrodes; they can also form during the electrochemical process of charging or discharging. In this feature article, the various solid–solid interfaces in porous electrodes are covered. In particular, by referring to studies in our group, a concept of a specific interfacial area is proposed, which provides an index to evaluate solid–solid interfacial interactions at the meso-scale; furthermore, two types of solid–solid interfacial interactions at the micro-scale, namely the van der Waals interface and the covalent interface, are discussed and compared in terms of their efficiency in electrocatalysis; empirical yet general guidelines for construction of solid–solid heterogeneous interfaces which support efficient interfacial electron transfer and electrocatalytic stability are provided accordingly. Last but not least, the role of interfacial electron delocalization behaviors in modulating the local electronic structure of the active sites and catalytic activity is emphasized. With this, this feature article aims to showcase the importance and charm of a solid–solid heterogeneous interface in regulating the efficiency of electrocatalysis.

Received 14th October 2024,  
Accepted 12th November 2024

DOI: 10.1039/d4cc05433d

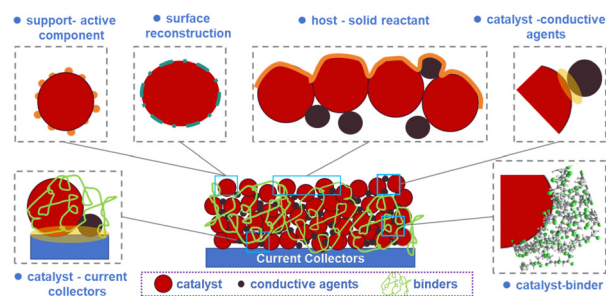
[rsc.li/chemcomm](http://rsc.li/chemcomm)

## 1. Introduction

Electrochemical catalysis has emerged as a pivotal field within chemical research, demonstrating significant potential for addressing environmental challenges and advancing energy conversion technologies. Its versatile applications in processes such as hydrogen production *via* water splitting, fuel cells, carbon dioxide reduction,<sup>1,2</sup> electrocatalytic synthesis of ammonia *via* N<sub>2</sub> or NO reduction,<sup>3,4</sup> the urea oxidation reaction (UOR),<sup>5</sup> metal–oxygen batteries<sup>6</sup> and the degradation of organic pollutants underscore its critical role in sustainable development initiatives. For any electrocatalytic process, the reaction kinetics, indexed by the overpotential at a specific current density, are determined by three types of polarizations, namely electrochemical polarization, ohmic polarization and concentration polarization. Historically, in an aqueous electrocatalytic

reaction, a solid–liquid interface between an electrocatalyst and an electrolyte has received the most attention most often; in general, the structure of the electrical double layer depends on the solid surface, the applied potential and the composition of the electrolyte.

Compared to a solid–liquid interface, a solid–solid heterogeneous interface receives much less attention in electrocatalysis. However, a solid–solid heterogeneous interface exists universally in a porous electrode. As shown in Scheme 1, the interface between a current collector and an electrode active material (which is usually a mixture of active nanoparticles (NPs) and conductive carbon granules being glued on a current



**Scheme 1** A schematic depiction of the various solid–solid interfaces existing in a porous electrode.

<sup>a</sup> College of Energy, Xiamen University, Xiamen 361005, Fujian, China.  
E-mail: [zhouy@xmu.edu.cn](mailto:zhouy@xmu.edu.cn)

<sup>b</sup> College of Chemistry and Chemical Engineering, Xiamen University, Xiamen 361005, Fujian, China

<sup>c</sup> School of Chemistry and Chemical Engineering of Hainan Normal University, Key Laboratory of Electrochemical Energy Storage and Energy Conversion of Hainan Province, Key Laboratory of Electrochemical Energy Storage and Light Energy Conversion Materials of Haikou City, Haikou, 571158, China

<sup>†</sup> These authors contributed equally to this work.

collector or a membrane) represents a typical example in this regard. The transfer of electrons across a heterogeneous interface is of paramount importance in redetermining the ohmic polarization, especially under large current density; the solid–solid interface robustness is also critical for the lifespan of an electrode, which sets high requirements on the long-term integrity of this solid–solid interface.<sup>7–9</sup>

At the heart of electrocatalytic processes lie catalysts.<sup>10,11</sup> Conventional electrocatalysts, such as metal, metal oxides and sulfides, are characterized by their good electrical conductivity, which enables efficient transfer of charge carriers.<sup>12–15</sup> However, to achieve a large electrochemically active surface area, active components have to exist as discrete NPs with low dimensions, and the electrical conductivity of the whole electrode can be an issue regardless of their high inherent electrical conductivity. The usage of additional conductive agents is thus necessary.<sup>16,17</sup> Meanwhile, for dispersion and stabilizing concerns, *e.g.*, when a noble metal is employed,<sup>18</sup> the usage of catalytic supports which are usually conductive carbon or semiconductors is also a necessity.<sup>19,20</sup> Within such a porous composite, there exists extensive contacts among the different solid particles, forming another type of solid–solid heterogeneous interface in addition to the one between the electrode active materials and the current collector; to accomplish low ohmic polarization, efficient interfacial transportation of charge carriers among the various discrete particles is also important.

Despite concerns on conductivity and dispersion, the solid–solid heterogeneous interaction provides an approach to modulate the local electronic structure of the catalytically active sites. In this scenario, a synergistic effect between the solid phases with different compositions which are rationally joined in space has often been reported. In this sense, an auxiliary solid (with respect to the catalytically active component) functions more than merely supporting or stabilizing the active component; it is also an electron modulator, which can donate to or withdraw electrons from the active solid depending on the factual work function between the two. One prominent example is the dispersion of metal-based NPs on carbon-based or other semiconductor-based materials.<sup>19,21</sup> This configuration not only enhances the spatial distribution of the metal NPs preventing agglomeration but also modulates the electronic structure of the catalytic sites through interfacial effects, leading to improved catalytic efficiency.<sup>22</sup>

Solid–solid interfaces can not only form during the synthesis of catalysts and the preparation of electrodes, but they can also form in an on-site manner during an electrochemical process (Scheme 1). Typical examples of this category are associated with the charging and discharging processes of batteries using a metal (*e.g.*, Li or zinc) as an anode. The cathode reactions during discharge usually involve electrocatalytic conversion of inorganic reactants (*e.g.*, O<sub>2</sub> or CO<sub>2</sub> or S<sub>8</sub> or I<sub>2</sub>) to the respective reducing state; during charge, the as-formed discharge products (*e.g.*, Li<sub>2</sub>O<sub>2</sub>, Li<sub>2</sub>CO<sub>3</sub>, amorphous carbon, Li<sub>2</sub>S *etc.*) would be electrocatalytically oxidized or decomposed. In these processes, either the reactants can exist collectively as solid

aggregates (*e.g.*, S<sub>8</sub> or I<sub>2</sub>), or the discharge products, which serve as the reactants in the charging process, are solids, taking for example Li<sub>2</sub>CO<sub>3</sub> formed in a Li–CO<sub>2</sub> battery and Li<sub>2</sub>O<sub>2</sub> formed in Li–O<sub>2</sub> or Li–air batteries.<sup>23–26</sup> Hence, the interfacial transfer of electrons between the conductive carbon and the solid reactant is of great importance for minimizing the discharge–charge potential gap or polarization.

On this basis, as can be seen, for electrocatalysis in both aqueous or organic media, solid–solid interactions occur universally due to the integration of two-phase or multiphase catalysts, the combination of catalysts with a conductive collector, or even between the catalyst and the solid reactant. To achieve efficient electronic interactions between two solids, in addition to the inherent work function of each solid, intuitively, the interfacial intimacy, which is determined by the surface roughness, the distance between the two surfaces, as well as the portion of interfacial atoms within the multiphase composite, shall also be carefully tuned; the local electronic structure of the interfacial atoms as well as the chemical affinity shall also be considered.

In this feature article, we present a review of research on electrocatalytic conversion of the various above-mentioned inorganic molecules in our group, with a focus on construction of solid–solid interfaces and exploration of their role in regulating the electrocatalytic activity. The factors affecting the solid–solid interaction strength were summarized. A straightforward but practically useful term, specific interface area (SIA), has been proposed, which depends on the geometry of two solids of concern as well as the way how they are being interfaced or positioned to each other. The SIA can be used to qualitatively evaluate the strength of the interfacial interaction; a larger SIA is associated with larger or more intensive interfacial interactions, which can serve as a guideline for efficient design of a solid–solid interface. The types of a solid–solid interface existing in an electrode and the different mechanisms through which they affect the electrocatalytic conversion of various inorganic molecules in both aqueous electrolytes and organic electrolytes are also covered by referring to typical examples in our research. The challenges and limitations of current research on this topic have also been discussed.

## 2. Structural features of solid–solid heterogeneous interfaces

### 2.1 Geometric concern at the meso-scale

A distinct characteristic between a solid and a liquid or a gas is that it has a clear and constant shape and also hardness or mechanical strength regardless of its size. While two solids can interact with each other easily through instantaneous physical contact,<sup>27–29</sup> it is often not easy or spontaneous for two solids to form a stable and intimate solid–solid interface. The reasons are obvious. To induce connection or bonds between the surface atoms of two solids, it requires not only the copresence of surface atoms of two phases but also places harsh requirements

on how they are sterically positioned with respect to each other, their surface topography, and surface activity. This can be relatively easily satisfied at the atomic or molecular scale for a solid–liquid or solid–gas interface, which however is challenging for a solid–solid interface since surface atoms in a solid suffer from much larger steric hindrance and lack of freedom compared to those in a fluent counterpart.

Intuitively, as shown in eqn (1), based on our various research examples, we propose that the intimacy and affluency of a solid–solid interface can be simply indicated by the specific interface area (SIA), which is the ratio of the interface area ( $S_{1-2}$ ) to the total mass of the two joined solids  $m_1$  and  $m_2$ , as shown in eqn (1).

$$\text{SIA} = S_{1-2}/(m_1 + m_2) \quad (1)$$

$$\text{SIA} = 1/(\rho_1 r_1 + \rho_2 r_2) \quad (2)$$

In an ideal case, for example, when the two adjacent solids assume a core–shell or layered configuration, the two solid surfaces are almost parallel to each other. As shown in Fig. 1a and eqn (2) where  $\rho$  is the density of the solid and  $r$  is the thickness of the solid in the direction normal to the interface, the so-called SIA in this case is inversely proportional to the thickness  $r$ . Straightforwardly, the thinner the active phase and the auxiliary phase are, the larger the SIA would be, and the stronger the interfacial interaction would be.

In reality, the SIA really depends not only on the dimension but also on the geometry and the configuration. Fig. 1b shows the various ways how two solids with different shapes can be interfaced with each other. Obviously, to achieve a large SIA, solids shall have a smaller size and low dimension, and two solids shall be parallel to each other, that is, the composite shall assume a core–shell or layered configuration. To this end, the solidification kinetics which involves nucleation and growth of the solids shall be optimized specifically depending on the individual research case.

## 2.2 Examples of inducing a large SIA for efficient conversion of inorganic small molecules

As simple as it is, this concept of SIA provides a general guideline to follow for design of electrocatalysts with solid–solid interfaces. As shown in Fig. 2a, for example, in the design

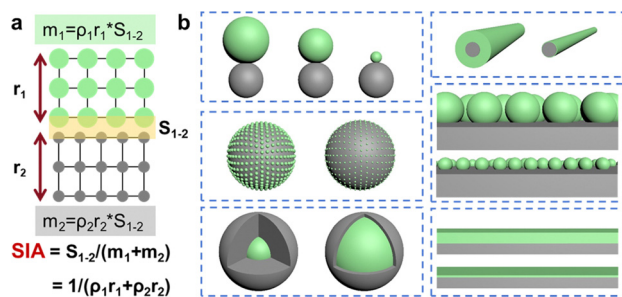


Fig. 1 (a) Depiction of the specific interface area (SIA) and (b) schemes showing the various solid–solid contact modes with different specific interface areas.

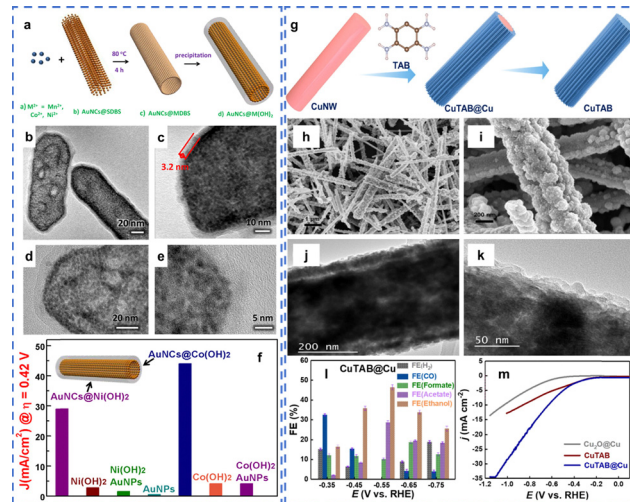


Fig. 2 (a) Synthesis of core–shell structured AuNCs@M(OH)<sub>2</sub>, (b)–(e) TEM images of AuNCs@M(OH)<sub>2</sub>, (f) current density at an overpotential of 0.42 V for the oxygen evolution reaction (OER) by AuNCs@M(OH)<sub>2</sub> and their comparisons,<sup>30</sup> (g) synthesis of CuTAB@Cu, (h) and (i) SEM, (j) and (k) HRTEM images of CuTAB@Cu, (l) faradaic efficiency (FE) of CuTAB@Cu, and (m) LSV profiles of CuTAB@Cu, CuTAB, and Cu<sub>2</sub>O@Cu.<sup>31</sup>

of metal hydroxide coated gold NPs (AuNCs@M(OH)<sub>2</sub>, M = Mn, Co, or Ni), the deposition kinetics of M(OH)<sub>2</sub> has been controlled so that their thickness can be controlled to be less than 4.0 nm (Fig. 2b–e). With a core–shell configuration and a thin amorphous layer, a large SIA can be obtained; as such, there exists a strong solid–solid interaction between the semiconductor M(OH)<sub>2</sub> and the assembled Au NPs, which have much higher conductivity and electronegativity that were found to enhance the electroactivity of Ni(OH)<sub>2</sub> and Co(OH)<sub>2</sub> towards the oxygen evolution reaction (Fig. 2f).<sup>30</sup>

Another similar example in this regard is a core–shell structured nanocomposite formed between the highly conductive Cu nanowire and the 1,2,4,5-tetraaminobenzene (TAB) (Fig. 2g).<sup>31</sup> Fig. 2h–k show the topography of CuTAB@Cu: bumpy aggregates of small NPs are observed on its surface, and the TEM observation further confirms the core–shell structure. The outside thin nanoshell is a CuN<sub>4</sub>-based CPP (Cu–TAB) polymer where Cu<sup>2+</sup> is tetra-coordinated *via* four dsp<sup>2</sup> hybrid orbitals with four N-containing groups in TAB. Though it possesses numerous Cu–N<sub>4</sub> sites which shall be active for electroreduction of CO<sub>2</sub>, bulky Cu–TAB aggregates showed little electrocatalytic activity. Interestingly, when being interfaced with metallic Cu nanowires, as shown in Fig. 2l and m, by carefully tuning the thickness of the Cu–TAB nanoshell, Cu–TAB becomes highly active and CO<sub>2</sub> is mainly converted to liquid products, with a FE of 46% towards ethanol at a potential of –0.55 V vs. RHE. The thickness of the Cu–TAB nanoshell was found to be important to enable high activity.

The above-mentioned SIA also provides the first guideline when designing electrocatalysts for metal batteries which involve conversion or formation of insulating solid reactants or products in the cathode during charge and discharge. A large SIA between the electrocatalyst (which is often a conductive

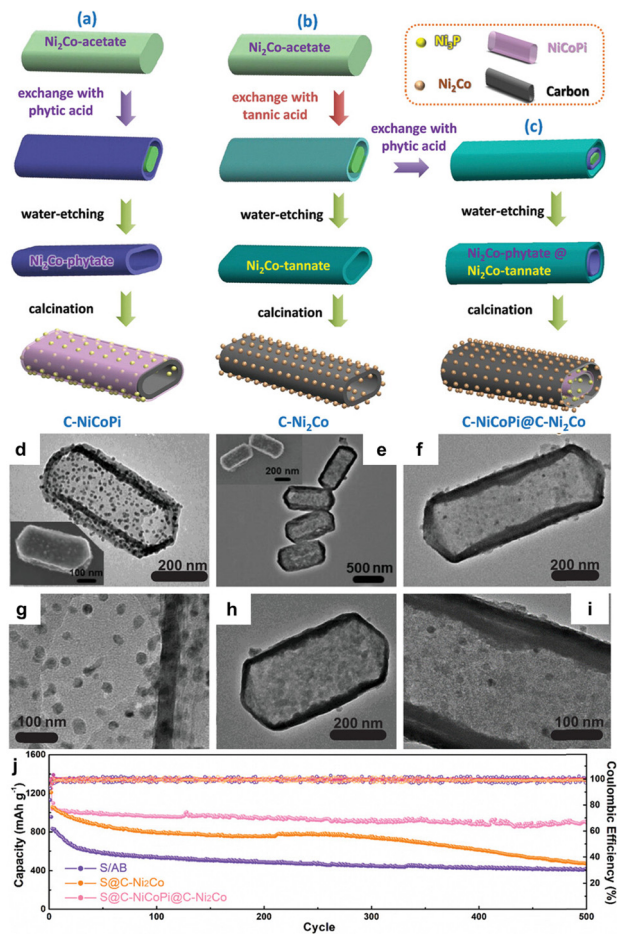


Fig. 3 Flowchart for design of (a) C-NiCoPi, (b) C-Ni<sub>2</sub>Co, and (c) C-NiCoPi@C-Ni<sub>2</sub>Co nanoshells, TEM images with different magnifications of: (d) and (g) C-Ni<sub>2</sub>Co nanoshell and the inset is the relevant SEM image, (e) and (h) C-NiCoPi nanoshell, (f) and (i) the bilayered C-NiCoPi@C-Ni<sub>2</sub>Co nanoshell loaded with elemental sulfur, and (j) charge-discharge cycling profiles at a current density of 0.5 C.<sup>24</sup>

carbon) and the reactant is necessary to ensure fast conversion kinetics and low polarization. In this scenario, the electrocatalyst actually serves as the host. To obtain high SIA, the host first of all shall have high specific surface area and large porosity to accommodate the insulating solid reactant and help dispersion of the insulating solid reactant.

Following such a guideline, carbonaceous hosts with large voids and ECSAs have been developed as cathode electrocatalysts for metal secondary batteries (e.g., Li-S batteries). Meanwhile, to address both the ohmic polarization as well as the electrochemical polarization, a non-polar carbon host can be interfaced with another polar or functional component, which together offer both electroconductivity and catalytic activity to the conversion of the insulating solid reactants during charging and/or discharging. As shown in Fig. 3a-c, by manipulating the anion-exchange process between Ni-Co acetate microcrystals and tannic acid or phytic acid, we have synthesized hollow porous single- or multi-layered hierarchically functionalized carbon nanoshells.<sup>24</sup> In particular, the shell-in-shell composite C-NiCoPi@C-Ni<sub>2</sub>Co has an external Ni<sub>2</sub>Co-decorated carbon

nanoshell and an internal Ni<sub>3</sub>P-anchored carbon nanoshell encapsulated within a continuous NiCo-phosphate (NiCoPi) layer (Fig. 3f and i). When solid sulfur is loaded into the host, in such a three-layered composite, the carbon nanoshell offers high electronic conductivity; the polar NiCoPi nanoshell offers not only mechanical stability but also catalytic activity in converting the different polysulfide intermediates; hence, both the ohmic polarization and electrochemical polarization can be reduced. Owing to the large void, the polar nature, and high conductivity, it displays collective merits as a sulfur host in Li-S batteries and maintains capacity retention as high as 86% after 500 cycles (Fig. 3j). In addition, we have also designed two-dimensional carbon nanosponge with a rich P-dopant (4.2 at%) and a large specific surface area (1966 m<sup>2</sup> g<sup>-1</sup>) in anchoring I<sub>2</sub>/I<sub>x</sub><sup>-</sup> (x = 1, 3 or 5) and catalyzing their mutual conversion in Zn-I<sub>2</sub> batteries.<sup>23</sup>

Notably, in some cases solid reactants such as Li<sub>2</sub>CO<sub>3</sub> and Li<sub>2</sub>O<sub>2</sub> are formed during the discharge of a secondary metal battery, in which the cathode host actually serves as the substrate for nucleation and growth of the as-formed solid discharge products; the lack of intimate atomic interactions at the solid-solid interface of the cathode can lead to excessive overpotential loss during charging.<sup>6</sup> In this situation, it is important to induce homogeneous deposition of the discharge products across the electrode to achieve a large SIA. Hence the solid-solid interfacial affinity is also important in addition to the aforementioned porosity and specific surface area, so that the morphology and dimension of the as-formed solid discharge product can be regulated. As the above solid discharge products are mostly polar in nature, in most cases, a metal-relevant moiety or a hybrid dopant is introduced into the carbon host to induce polarity, so as to enhance the interaction between the host and the solid reactants. Some studies have also shown that the compositions of the electrolyte can also mediate the growth of discharge products in metal-O<sub>2</sub> battery systems.<sup>6</sup>

Examples in this regard are shown in Fig. 4. To guide and accommodate the discharge solid product (Li<sub>2</sub>O<sub>2</sub>) for Li-O<sub>2</sub> batteries, we have developed a flexible and integrally bilayered CNT-based cathode by *in situ* growing a layer of numerous microflower-shaped assembly of cobalt nanoparticle-embedded nitrogen-doped carbon nanotubes (CNTs) on a flexible current collector which is also a CNT-interwoven film (Film<sub>CNTs</sub>) (Fig. 4a).<sup>25</sup> Such an integrally bilayered cathode (Flower<sub>CNTs</sub>@Film<sub>CNTs</sub>) is not only freestanding and highly porous, but also possesses high electronic conductivity and electrocatalytic activity (Fig. 4b and c); as such, it can support fast oxygen reduction and ensure uniform dispersion of the insulating solid product Li<sub>2</sub>O<sub>2</sub> during the discharge process; during the charge process, as it can support efficient electron transfer across the intimate solid-solid interfaces, including the one between the catalyst layer and current collector and the one between Li<sub>2</sub>O<sub>2</sub> and the catalytic active sites, it enables fast and thorough decomposition of Li<sub>2</sub>O<sub>2</sub> (Fig. 4d). In comparison, in the control sample where carbon nanotubes were being scattered on the CNT-interwoven film, large aggregates of

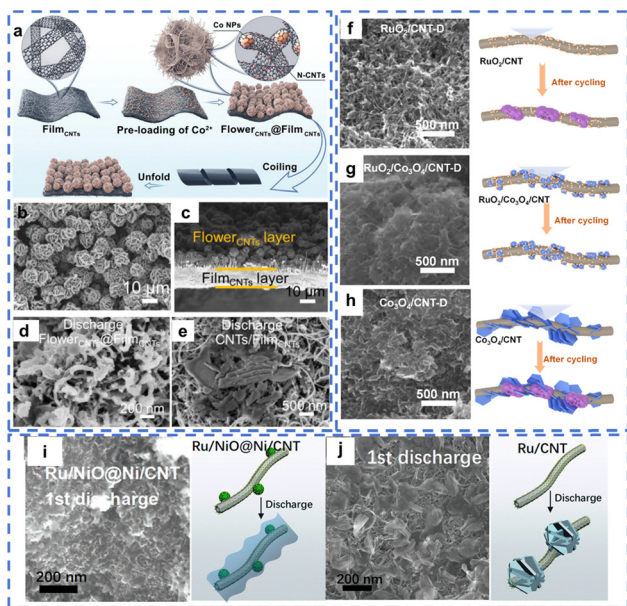


Fig. 4 (a) Flow chart for preparation of Flower<sub>CNTs</sub>@Film<sub>CNTs</sub>, (b)–(e) SEM images of fresh/discharged Flower<sub>CNTs</sub>@Film<sub>CNTs</sub> electrode and discharged CNTs/Film<sub>CNTs</sub> electrode;<sup>25</sup> (f)–(h) SEM images and schematic drawings of discharged RuO<sub>2</sub>/CNT, RuO<sub>2</sub>/Co<sub>3</sub>O<sub>4</sub>/CNT, Co<sub>3</sub>O<sub>4</sub>/CNT electrode;<sup>26</sup> and (i) and (j) Ru/NiO@Ni/CNT and Ru/CNT cathode.<sup>32</sup>

Li<sub>2</sub>O<sub>2</sub> were formed, which resulted in severe polarization during charging (Fig. 4e).<sup>25</sup>

Another example is the design of RuO<sub>2</sub>–Co<sub>3</sub>O<sub>4</sub>/CNT as a cathode for Li–CO<sub>2</sub>/O<sub>2</sub> batteries with long-term stability. The strong interfacial interaction between RuO<sub>2</sub> and Co<sub>3</sub>O<sub>4</sub> was found to modulate the morphology of Li<sub>2</sub>CO<sub>3</sub> formed during discharging.<sup>26</sup> The copresence of RuO<sub>2</sub>–Co<sub>3</sub>O<sub>4</sub>/CNT was found to guide the morphology of the insulating Li<sub>2</sub>CO<sub>3</sub>, which existed as a thin layer of membrane-like morphology, coating on the CNTs in a relatively homogeneous way (Fig. 4g). Both the SEM observation and XRD profiles confirm complete decomposition of Li<sub>2</sub>CO<sub>3</sub> after charging when RuO<sub>2</sub>–Co<sub>3</sub>O<sub>4</sub>/CNT was employed as the electrocatalyst, whereas accumulation of Li<sub>2</sub>CO<sub>3</sub> after charging was observed when RuO<sub>2</sub>/CNT or Co<sub>3</sub>O<sub>4</sub>/CNT was used (Fig. 4f and h). The decomposition kinetics of Li<sub>2</sub>CO<sub>3</sub> was also accelerated by the solid–solid interaction between RuO<sub>2</sub>–Co<sub>3</sub>O<sub>4</sub>, according to DFT calculations.<sup>26</sup> In another similar study, as shown in Fig. 4i and j, we also noticed that Li<sub>2</sub>CO<sub>3</sub> formed in Li–CO<sub>2</sub>/O<sub>2</sub> on Ru/CNTs tends to exist as a bulky aggregate (Fig. 4j); when a Ni-based moiety is introduced, *e.g.*, for a Ru/NiO@Ni/CNT, Li<sub>2</sub>CO<sub>3</sub> would form in a more uniform way around the CNTs (Fig. 4i), leading to relatively large SIA, which decreases the polarization and is beneficial for the long-term stability.<sup>32</sup>

In addition to the surface properties of a cathode electrocatalyst, we also found that the reaction kinetics can be modulated by the composition of the gas or the addition of functional additives into the electrolyte, which also provides an opportunity to tune the SIA between the electrocatalyst and the resulting solid discharge product.<sup>33,34</sup> For instance, recently, we reported that the presence of trace amounts of ferrocene

(an organic transition metal compound with aromatic properties) in an electrolyte can stabilize the discharge intermediates and favor the occurrence of the two-electron reaction path during the CO<sub>2</sub>RR in the discharge; meanwhile, it has a relatively high adsorption capacity for CO<sub>2</sub> and can affect the solvation environment of Li<sup>+</sup>, which will shorten the path of CO<sub>2</sub> binding to Li<sup>+</sup> at the reaction interface during the discharge process, promoting the uniform nucleation of discharge products, thereby significantly increasing the discharge capacity.<sup>35</sup>

### 2.3 Types of interactions at solid–solid heterogeneous interfaces

While the SIA is an important index to evaluate the strength and extensiveness of the solid–solid interaction at the meso-scale, another important factor at the micro-scale is the surface property, including the saturation level or the coordination number of surface atoms and the chemical affinity. In this regard, depending on the type of forces which join or connect the two solid surfaces, it falls into two types, the van der Waals (VdW) interface and the covalent bonding interface.

VdW interfaces, as their name goes, rely on the van der Waals forces, which include Keesom, Debye, and London forces, typically exhibiting strengths in the range of 0.1–10 kJ mol<sup>−1</sup>.<sup>36</sup> Regardless of the ease in thermodynamics and their universal existence, two solids, or two surfaces, shall be close enough to each other, to approach the so-called VdW distances,<sup>37</sup> as van der Waals forces would decrease or even vanish with increasing distance between any two objects. In this sense, the surface roughness of the two surfaces shall be concerned, so as to enable the most atoms in two adjacent surfaces to be close to each other at the atomic scale. The population of atoms involved in the interaction shall also be proportionally positive to the adhesion strength. Hence, a solid–solid interface with larger SIA shall be associated with stronger van der Waals forces. It shall also be clarified that, because of the constraints on the inter-surface distance as well as the small SIA, it is hard to form an efficient or strong van der Waals interface for two bulky solids.

It is thus understandable that a VdW interface might form easily between two solids with low dimensions. The collector is typically a two-dimensional material, while the catalyst can vary in dimensionality; VdW forces play an important role in the physical stability and distribution of catalyst particles on collectors. Weaker VdW interactions may lead to issues such as catalyst detachment and aggregation, which can impair the effective usability of the catalyst.

A strategy to increase the van der Waals forces between the catalyst and the current is to construct a binder-free electrode where the catalyst layer is deposited or grown on the current collector directly through an *in situ* manner. During the preparation of such an electrode, to form the catalyst layer, the nucleation takes place on the current collector (which is usually carbon fibers or a metal piece); this can minimize the inter-layer distance or gap between the as-formed catalyst layer and the current collector. Nevertheless, the weak nature of

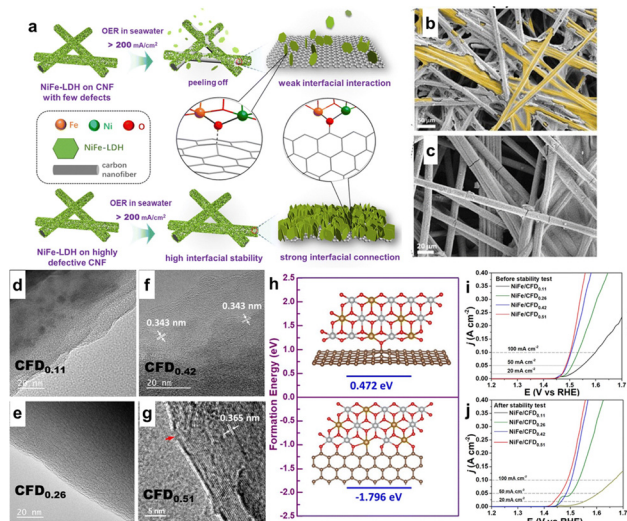


**Fig. 5** (a) A scheme to compare the catalytic stability of the van der Waals interface and the covalent interface between the NiFe-LDH-based electrocatalyst and the carbon-based current collector, (b) SEM images of the spent NiFe/CFD<sub>0.11</sub> and (c) the NiFe/CFD<sub>0.51</sub> after long-term seawater electrolysis, (d)–(g) TEM images of the bare carbon fabrics with different levels of defects (namely CFD<sub>r</sub>), (h) DFT calculations of the solid–solid interfacial bonding energy between NiFe-LDH and carbon in different locations, and (i) and (j) OER LSV profiles of the four NiFe/CFD<sub>r</sub> before and after the stability test.<sup>38</sup>

interlayer VdW interactions presents challenges in regulating the interfacial charge transfer as well as the long-term stability. A typical example we have demonstrated in this regard is the oxidation of seawater. As shown in Fig. 5a, the interface between the NiFe-LDH layer and the pristine carbon current collector is dominated by van der Waals forces, which can not resist the etching of halide anions to the catalyst; leakage of metal cations at the interface consequently leads to catalyst peeling off (Fig. 5b).<sup>38</sup> This is because that, under highly positive applied voltage, the halide anions are highly concentrated on the anode, which can coordinate with the metal cations, leading to leakage of metal cations.

In addition to VdW forces, it shall also be mentioned that in some cases other intermolecular forces such as  $\pi$ – $\pi$  stacking and hydrogen bonding can also be introduced to strengthen a VdW solid–solid interface.<sup>39,40</sup> These interactions can also help to facilitate charge transfer between two solids thereby enhancing the electrochemical properties of the composite. However, different from the universal VdW forces, to induce  $\pi$ – $\pi$  stacking<sup>41,42</sup> and hydrogen bonding,<sup>43</sup> it not only requires the two solid surfaces in close proximity, but also sets requirement on the chemical compositions of the two surfaces, which hence is not discussed in detail in this review.

Compared to the VdW interface, covalent bonding formed through sharing of electron pairs between atoms located separately in two surfaces renders a much stronger interaction between two solids, which typically exhibits strength two to three orders of magnitude higher than that of VdW interfaces (100–1000 kJ mol<sup>−1</sup>). Hence, covalent bonds are more resilient, exhibiting higher stability and resistance to mechanical stress

and chemical corrosion.<sup>44</sup> This provides structural integrity, minimizes catalyst detachment or migration, and suppress undesired side reactions during operation. Meanwhile, these strong covalent bonds also facilitate efficient electron transfer at the interface, which can reduce the internal resistance and thus improve the electrochemical activity of the catalyst.<sup>45</sup>

The formation of interfacial covalent bonds is influenced by the chemical coordination capability of the interface atoms.<sup>38</sup> As shown in Fig. 5d–g, by steam etching of the carbon fiber, its defect density can be tuned, and this carbonaceous current collector with higher defect density tends to form interfacial C–O–M covalent bonds with the metal sites of the NiFe-LDHs nanosheets. The interaction between the edge dangling M–O sites (M = Ni or Fe) in NiFe-LDH and the carbon sites in different locations was simulated by calculating the Gibbs energy associated with the formation of an interfacial oxygen bridge, that is, the covalent bonding C–O–M; it was obtained as 0.472 eV for the carbon atom located within a typical two-dimensional graphitic plane (Fig. 5h), which is −1.796 eV for the edge C atoms which represent a typical kind of defect. Owing to the extensive existence of the interfacial oxygen bridges (namely C–O–M) between the NiFe-LDH nanosheets and the defective carbon fiber; the electrocatalyst peeling off, which is caused by coordinative etching of the concentrated chloride anions at the interface, is effectively suppressed during seawater oxidation (Fig. 5c). It also reduces the ohmic contact impedance between the electrocatalyst and the collector, improving the apparent electrocatalytic activity of the electrode (Fig. 5i and j).

Another typical example also discovered by our research is the nanocomposite formed between the FeOOH NPs and the Ni–Fe LDH nanosheets.<sup>46</sup> As shown in Fig. 6a, using the stainless steel NPs as an iron source, FeOOH NPs with average size around 2.0 nm were deposited on NiFe-LDH nanosheets (Fig. 6c–e); two control samples were also prepared by a step-wise hydrothermal method (Fig. 6b), where FeOOH NPs with an average size of 18.0 and 10.0 nm were deposited on the NiFe-LDH nanosheets (Fig. 6f–k), respectively. We reported that, compared to the bare NiFe-LDH, the loading of FeOOH NPs

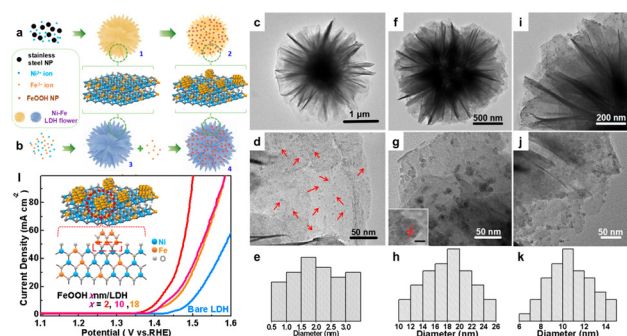


**Fig. 6** (a) One-pot synthesis of the FeOOH<sub>2nm</sub>/LDH composite; (b) step-wise synthesis of FeOOH/LDH, TEM images and size distributions of (c)–(e) FeOOH<sub>2nm</sub>/LDH, (f)–(h) FeOOH<sub>18nm</sub>/LDH, (i)–(k) FeOOH<sub>10nm</sub>/LDH, and (l) LSV curves of various samples for the OER and schematic depiction of the interfacial oxygen bridges between the FeOOH NPs with Ni–Fe LDH.<sup>37</sup>

obviously enhances the OER electrocatalytic activity. Such a synergistic effect depends on the size of FeOOH; when the average size of FeOOH NPs decreased from 18.0 nm to 2.0 nm, the overpotential at 10 mA cm<sup>2</sup> decreases obviously (Fig. 6l). We speculated that FeOOH NPs with an average size of 2.0 nm are highly unsaturated, and thus tend to form interfacial oxygen bridges (namely Fe–O–Ni) with the NiFe-LDH substrate; the thus formed bimetal pairs possess high-oxidative-state Fe<sup>(3+δ)+</sup> sites and a relatively short Fe<sup>(3+δ)+</sup>–O bond, which favor a faster oxygen evolution reaction.

It shall also be pointed out that, as the fresh electrocatalysts are actually pre-catalysts which usually undergo structural reconstruction, a new solid phase actually forms the existing matrix. In this scenario, it is reasonable to speculate that the as-generated solid–solid interface exists as a covalent interface. A relevant example is the formation of NiOOH from a metal hydroxide matrix during the alkaline OER. Our team found that the structural evolution of the pre-existing cationic defects in the fresh pre-catalysts (*e.g.*, NiFe-LDHs) and electrocatalyst surface reconstruction are like two sides of the same coin (Fig. 7a).<sup>47</sup> Specifically, the simple cationic vacancy defects V<sub>M</sub> in the precatalyst would transform into a relatively complicated configuration such as V<sub>MOH</sub> and eventually V<sub>MOH-H</sub> (Fig. 7b). As shown in Fig. 7c–f, the *in situ* Raman results further clarify the role of the cation defects of the catalyst, the V<sub>MOH-H</sub> in stoichiometry corresponds to the formation of NiOOH. This is a relatively early study which investigated the

relationship between the formation of the new active phase with the structural defects in the matrix precatalyst. This surface reconstruction process has also been employed to transform the various transition metal cations adsorbed on carboxylic-functionalized Ni-doped ALOOH nanoflowers (ALOHH NFs) into the relevant MOOH NPs (Fig. 7g). As shown in Fig. 7h and i, we synthesized Ni-doped ALOOH NFs by a one-pot method, which then was explored as an electrocatalyst for the OER.<sup>48</sup>

Another example involving the on-site formation of solid–solid interfaces during electrocatalysis is electrocatalytic oxidation of urea (UOR), though it is often used to replace the OER to reduce the anodic potential for hydrogen production from water reduction owing to its relatively lower potential. For instance, Ting *et al.* synthesized a (NiFeCo)<sub>x</sub>/FeOOH/NiFeCo(OH)<sub>x</sub> heterostructure (Fig. 8a–e) on a foam nickel substrate.<sup>5</sup> As a UOR electrocatalyst, it exhibits excellent electrochemical activity and stability (Fig. 8f and g). Transition metal sulfide commonly shows good electrical conductivity and rapid *in situ* electrochemical reconstruction due to the higher

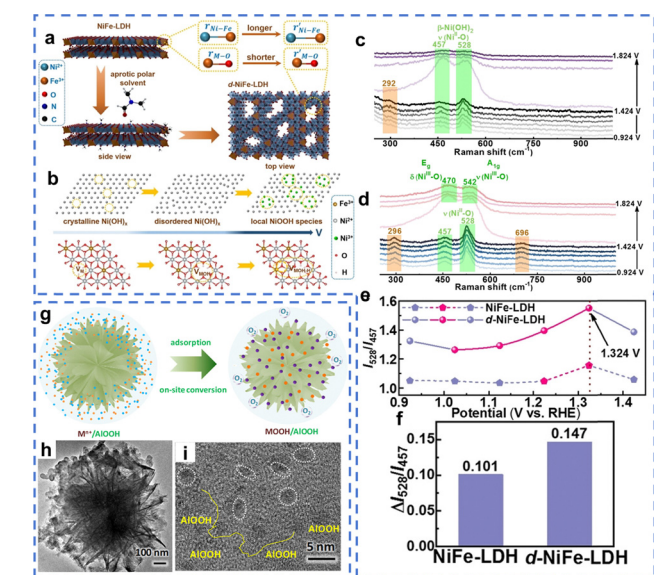


Fig. 7 (a) The coordination between the aprotic polar solvent DMF and cations in NiFe-LDH leading to the dissolution of the metal cations and formation of defective NiFe-LDH, (b) local conversion of crystalline Ni(OH)<sub>x</sub> species to their disordered or defective status, *in situ* Raman spectra of (c) the pristine NiFe-LDH and (d) d-NiFe-LDH in OER electrocatalysis, (e) the evolution of I<sub>528</sub>/I<sub>457</sub> versus potential; (f) ΔI<sub>528</sub>/I<sub>457</sub> of NiFe-LDH and d-NiFe-LDH;<sup>47</sup> (g) surface reconstruction of transition metal cations adsorbed on N-doped ALOOH NFs surfaces, and (h) and (i) TEM and HRTEM images of Ni-doped ALOOH NFs after surface reconstruction.<sup>48</sup>

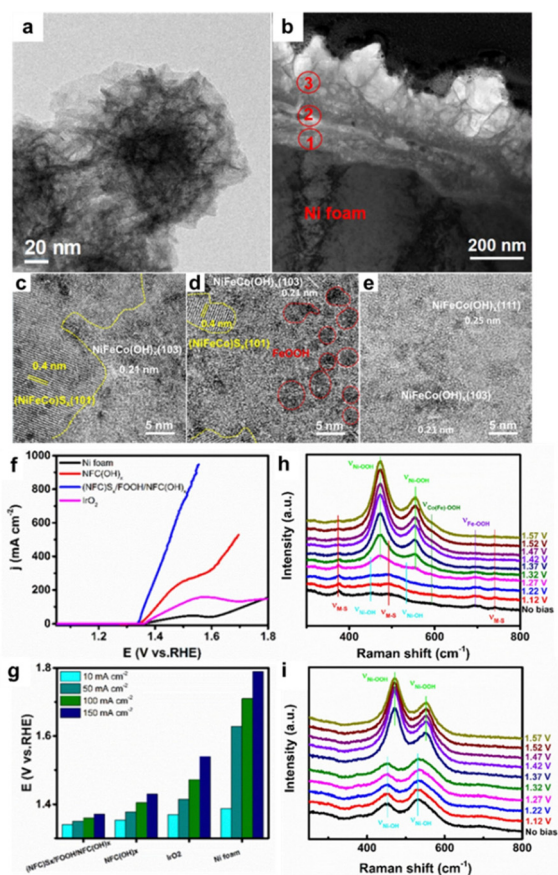


Fig. 8 Electro-oxidation of urea by (NiFeCo)<sub>x</sub>/FeOOH/NiFeCo(OH)<sub>x</sub>: (a) top-view and (b) cross-sectional TEM images of the electrocatalyst, HRTEM images of (c) the bottom layer, (d) middle layer, and (e) top layer in (b); comparison of different catalysts for urea electrooxidation: (f) the relevant polarization LSV curves and (g) the potential at different current densities; and *operando* Raman spectra of (h) (NiFeCo)<sub>x</sub>/FeOOH/NiFeCo(OH)<sub>x</sub> and (i) NiFeCo(OH)<sub>x</sub>.<sup>5</sup>

polarization ability and lower electronegativity of S compared to those of O. Consequently, during the UOR,  $(\text{NiFeCo})\text{S}_x$  also gradually transforms into metal (oxy)hydroxide during the UOR, providing additional active species. This is supported by *in situ* Raman spectroscopic observation which reveals the formation of  $\text{NiOOH}$  (Fig. 8h and i). Multiple heterogeneous interfaces induce local electron modification structures that delocalize the D-band center, thereby affecting the bond strength between the catalyst and the intermediates generated during the UOR process.<sup>5</sup>

### 3. Synergistic effect of solid–solid interfaces in tuning electrocatalytic activity

As shown repetitively in the afore-discussed examples, a major function of the various solid–solid interfaces within the electrode, taking those formed between the electrocatalyst and the current collector for example, is to support efficient cross-interfacial transfer of electrons which hence is critical to achieve low ohmic polarization.

In addition to the interfacial transfer of electrons, our research emphasizes the synergistic effect of the auxiliary phase in modulating the local electronic structure of the active phase. The rationale is that, when the two solids with different work functions are interfaced with each other, similar to a heterojunction, a so-called space charge layer would be built up around the interface, modulating the electron energy distribution and influencing the upward or downward bending of the energy bands nearby.<sup>49</sup> The resultant space charge layer, characterized by an uneven charge density, often extends beyond the physical interface; its thickness varies depending on the materials' electrical properties – thinner for highly conductive materials and broader for those with lower conductivity. When a metal and a semiconductor are in contact, the free electrons will transfer between the metal and semiconductor due to the work function difference.<sup>50</sup>

To induce a synergistic effect between the auxiliary phase and the active phase *via* such an interfacial interaction, the interfacial charge transfer shall be optimized to elevate the electrocatalytic efficacy of the active sites. To this end, three conditions shall be at least satisfied. First, the two joined solids shall have large SIA and shall be a covalent solid–solid interface. Second, careful consideration shall be given to their physical and/or chemical properties, including their conductivity and electronegativity. Additionally, the size and thickness of the active phase should be minimized to amplify the SIA, ensuring that active sites are strategically located within the space charge layer to exploit the charge transfer dynamics effectively. Optimizing these parameters can significantly enhance catalyst performance.<sup>51–54</sup>

The combination of a metal-based NP or a graphitic carbon has been mostly explored. In one of our early studies, a porous hollow carbon nanoshell was prepared, in which  $\text{FeN}_x$  and  $\text{CoN}_x$  metal sites are atomically dispersed and interfaced

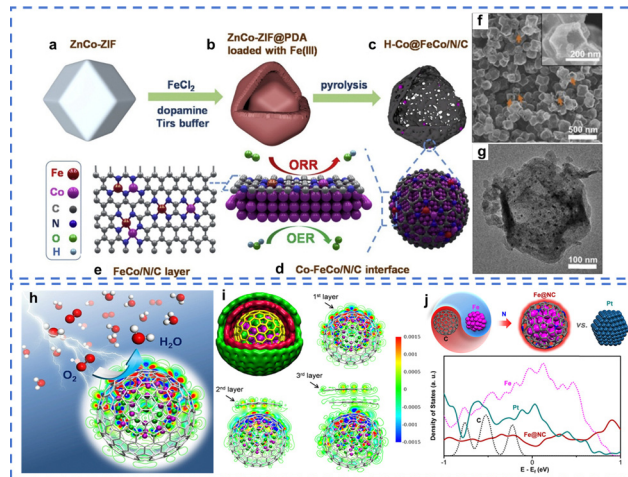


Fig. 9 (a)–(e) A flowchart showing the synthesis of H-Co@FeCo/N/C, and the metal–carbon solid–solid interface between the metallic Co NP and the FeCo/N/C layer. (f) SEM and (g) TEM images of H-Co@FeCo/N/C;<sup>55</sup> (h) a diagram showing the ORR process on a chainmail electrocatalyst, (i) interfacial charge redistribution in chainmail catalysts with different graphene layers, and (j) a model of Fe@N-doped C chainmail catalyst mimicking the electronic properties of Pt near the Fermi level.<sup>56</sup>

intimately with metallic Co NPs (Fig. 9a–e). Such H-Co@FeCo/N/C displays a rhombic dodecahedron shape (Fig. 9f and g); many of them are perforated and exhibit high surface roughness. They served as efficient bifunctional electrocatalysts for the ORR and the OER in Zn–air batteries.<sup>55</sup> Though solid–solid interfacial electronic interactions were not discussed in this study, relevant studies later indicate that such an interfacial electronic interaction is unavoidable. In this regard, the concept of “armored catalysis” represents typical examples showing the significance of the interfacial electron transfer between a thin graphitic layer and a metal NP.<sup>56,57</sup> In such armored catalysts, metal NPs are encapsulated within a thin layer of carbonaceous materials; there exists interfacial electron transfer from the metal to the carbon matrix, which not only stabilizes the NPs but also engenders a distinctive catalytic activity at the carbon surface.<sup>56,57</sup> As exemplified in Fig. 9h, the Fe NP inside a carbon nanotube can form covalent bonds with carbon owing to overlapping of the Fe 3d and C 2p states; such interfacial electronic interactions as well as the induced charge redistribution then activates the carbon layer on which the adsorption and dissociation of  $\text{O}_2$  is facilitated in the case of the ORR; it has also been found that the interfacial electron redistribution behaviors are sensitive to the thickness of the carbon coating layer; in general, a layer number less than three favors stronger interaction with the metal-based NPs (Fig. 9i). The combination of the electronic states of the chainmail layer and the metal cores can even be used to mimic the electronic structures of noble metal catalysts, such as Pt, to improve their catalytic properties (Fig. 9j).<sup>56</sup>

The afore-discussed CuTAB@Cu is also a typical example showing the charm of interfacial electron transfer in regulating the efficacy of the active sites.<sup>31</sup> Based on XPS and XAFS analysis, there exists transfer or delocalization of electrons

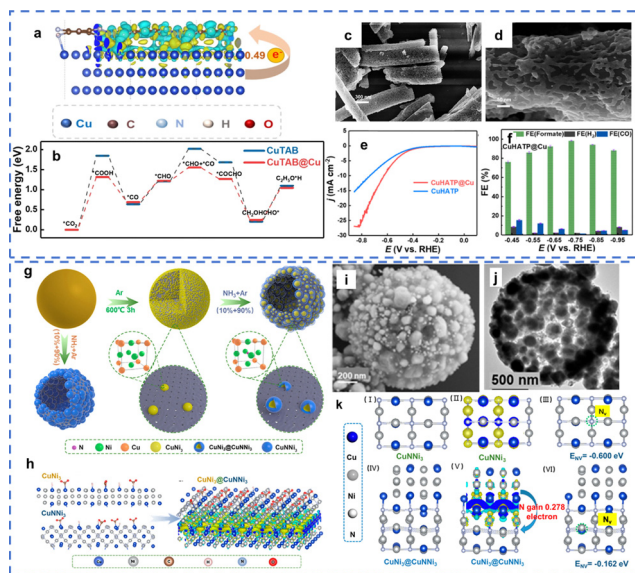


Fig. 10 (a) Charge density difference of the hybrid, comparison of (b) free energy diagrams for the  $\text{CO}_2\text{RR}$ , (c) and (d) SEM image of  $\text{CuHATP@Cu}$ , (e) LSV profiles of  $\text{CuHATP@Cu}$ , (f) FE of the  $\text{CO}_2\text{RR}$  catalyzed by  $\text{CuHATP@Cu}$ .<sup>51</sup> (g) flowchart of synthesis of the assemblage of core-shell-structured nanocomposites and (h) cartoon depiction to show differentiated adsorption behaviors of  $\text{CO}_2$  and  $\text{H}^+$ , (i) and (j) SEM and TEM image of  $\text{CuNi}_3\text{@CuNNi}_3/\text{C}$ , and (k) DFT calculation results of the N element escape energies in pure  $\text{CuNNi}_3$  crystals and in  $\text{CuNNi}_3$  being interfaced with  $\text{CuNi}_3$ .<sup>58</sup>

from the metallic Cu nanowire to the thin CuTAB nanoshell, which enriches the local electronic density of affluent  $\text{CuN}_4$  sites within the CuTAB nanoshell and endows it with high  $\text{CO}_2$  electroreduction activity. DFT calculations revealed that there exists transfer of 0.49 electrons from the Cu nanowire core to the CuTAB nanoshell, which effectively decreases the energy barrier for generation of a  $^*\text{COOH}$  intermediate, as shown in Fig. 10a and b. A similar phenomenon was also observed when another conjugated coordination polymer Cu-HATP (where HATP refers to 2,3,6,7,10,11-hexaaminotriphenylene) was coated on copper nanowires, as shown in Fig. 10c and d. From the LSV polarization curves it can be seen that the current density of  $\text{CuHATP@Cu}$  is greater than that of CuHATP throughout the potential window (Fig. 10e) and the FE of formic acid can reach 97.8% (Fig. 10f).

Another interesting example on interfacial electron delocalization between two joined solids discovered in our group is the  $\text{CuNi}_3\text{@CuNNi}_3/\text{C}$  nanocomposite (Fig. 10g and h).<sup>58</sup> Fig. 10i and j display the morphology of the  $\text{CuNi}_3\text{@CuNNi}_3/\text{C}$  series catalysts. In the primary NPs, a thin layer of  $\text{CuNNi}_3$  (which is a type of anti-perovskite material) is coated on  $\text{CuNi}_3$  alloy NPs. Compared to the bulky  $\text{CuNNi}_3$ , due to the interfacial interaction, thermal stability and electrocatalytic stability of  $\text{CuNNi}_3\text{@CuNi}_3$  during the  $\text{CO}_2\text{RR}$  are both improved obviously. Calculation of interfacial interactions between  $\text{CuNi}_3$  and  $\text{CuNNi}_3$  revealed transfer of electrons from the  $\text{CuNi}_3$  alloy core to the  $\text{CuNNi}_3$  nanoshell, which increases the N escape energy in the cubic cell of  $\text{CuNNi}_3$  and consequently enhances its chemical stability (Fig. 10k).

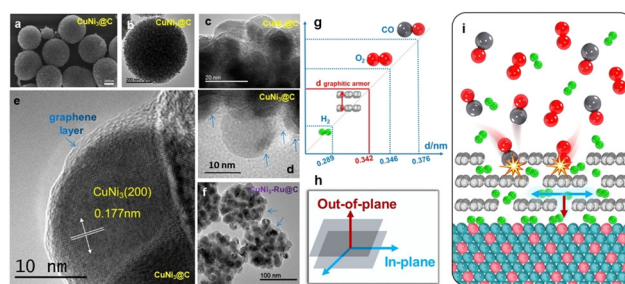


Fig. 11 (a) SEM and (b)–(e) TEM images with different magnifications of  $\text{CuNi}_3\text{@C}$ , (f) TEM image of  $\text{CuNi}_3\text{-Ru@C}$ , (g) a comparison of the sizes of various molecules and the space between layers in a graphitic armor, (h) a diagram illustrating two directions in the graphitic carbon layer, and (i)  $\text{CO}$  and  $\text{O}_2$  cannot diffuse in the plane of the graphitic armor, while  $\text{H}_2$  can move both in-plane and out-of-plane.<sup>59</sup>

In addition to the above electronic effect, recently, we also discovered that the solid–solid interface may function in another way. For instance, we found that the defective graphitic carbon, with a unique interlayer gap of 0.342 nm, can be a highly selective natural molecular sieve in hydrogen electro-oxidation.<sup>59</sup> Fig. 11a–e show that  $\text{CuNi}_3\text{@C}$  is a sphere made of graphitic carbon-coated  $\text{CuNi}_3$  NPs. The spaces between the NPs are filled with graphitic carbon (blue arrows in Fig. 11d). Shown in Fig. 11f,  $\text{CuNi}_3\text{-Ru@C}$  is also an assembly of numerous  $\text{CuNi}_3$  and metallic ultrafine Ru NPs being encapsulated within a graphitic armor. It allows efficient diffusion of hydrogen molecules or radicals both along the in-plane and out-of-plane directions, but sterically hinders the diffusion of molecules with a larger kinetic diameter (*e.g.*,  $\text{CO}$  and  $\text{O}_2$ ) along the in-plane direction (Fig. 11g–i). As a result, poisonous species larger than 0.342 nm are sieved out, even when their adsorption on the metal is thermodynamically strong (Fig. 11g and i). This natural molecular sieve provides a very chance for constructing robust metal catalysts for hydrogen-relevant processes, which are more tolerant to chemical or electrochemical oxidation or  $\text{CO}$ -relevant poisoning.

## 4. Conclusion and perspectives

While a solid–liquid interface in an electrochemical process has been the hotspot of research in electrochemistry, solid–solid heterogeneous interfaces exist universally in electrodes, which however somehow have been long overlooked compared to solid–liquid interfaces. In summary, this review or reflection of the various individual research examples in our group highlights the following three major aspects regarding the role of a solid–solid interface in electrocatalysis, and this can be enlightening for relevant researchers, especially beginners in this field:

(a) The importance of a solid–solid interface in electrocatalysis shall be recognized: a solid–solid interface can form during the synthesis of an electrocatalyst (*e.g.*, between the support and the active solid component), or preparation of an electrode (*e.g.*, among the conductive carbon granules and the

electrocatalyst particles, between the electrocatalyst layer and current collector). Efficient solid–solid interfacial interaction is necessary to ensure interfacial transfer of charge carriers as well as to guarantee long-term electrode integrity, especially when an electrochemical process is conducted in a chemically corrosive environment; interfacial electron delocalization at a solid–solid interface also provides an effective method to strategically modulate the local electronic structure and consequently the catalytic activity of the active sites.

(b) To achieve an extensive and intimate solid–solid interaction between two solids (which is often important for efficient electron transfer in electrocatalysis), our different research examples reveal that, at the meso-scale, the two interfaced solids shall have a large specific interfacial area, which sets requirement on the dimension of the two solids as well as on the way how they are being interfaced; at the micro-scale, a covalent solid–solid interface is preferred to achieve a strong interfacial interaction and a stable solid–solid interface, which requires careful tuning of the geometry as well the physicochemical properties of the surface atoms. This provides general guidelines and showcases to the readers how an efficient or optimal solid–solid interface shall be achieved in an electrocatalytic process.

(c) Last but not least, our research studies have also demonstrated the occurrence of the subtle interfacial electron delocalization phenomenon upon a solid–solid interface; how such an interfacial electronic interaction can modulate or even rewrite the physicochemical property of the electrocatalytic active sites during the electrochemical process has also been observed. Such a strong solid–solid interface electronic interaction, which thermodynamically shall be not easy, reveals the charm and potential of designing composite nanomaterials that leverage the unique properties of different components for realizing synergistic effects.

At the same time, while numerous research has demonstrated the importance and efficiency of solid–solid interfacial interactions in the electrocatalytic process, there are challenges when it comes to clarification of the structure–activity relationship. It's challenging to directly study the solid–solid interface because it's buried under a solid layer, which makes it hard to access. This makes it even more difficult to examine the electronic interactions happening at the interface. So far, we still have to rely on traditional *ex situ* or *in situ* characterization techniques such as SEM, TEM, AFM, XPS, XRD, and Raman spectroscopy. These methods, while useful for assessing the surface morphology, internal structure, and chemical states, often fall short when it comes to capturing the dynamic nature of solid–solid interfacial interactions which often locate underneath the reactive solid–liquid interface during reactions. The intricate three-dimensional architecture of these interfaces, coupled with their dynamic changes during electrochemical reactions, thus cannot be fully resolved using conventional techniques, thereby limiting our understanding of how these interfaces influence electrocatalytic performance.

Meanwhile, design of control samples is usually important for accurate comparison of electrocatalytic performance. An

efficient control sample shall be able to support the so-called single-variable experiment. However, as the composite usually exists as nanomaterials, the design of efficient control samples is particularly challenging. It is often hard or even impossible to delicately change only one structural parameter (*e.g.*, the thickness of the active solid) and at the same time not change the other structural features of the solid. Structural features such as the dimension, the surface structure, and the crystallinity of both solids might change at the same time when synthetic conditions are varied. The complexity of these systems, combined with the need to control multiple variables, makes it difficult to generate consistent and reproducible results. In this sense, data interpretation shall be cautioned.

At the current stage, to prove the interfacial electronic interaction, we often have to resort to DFT calculations, which, however, do not necessarily depict the real sample. This gap between the theoretical calculations and the real catalyst design is yet to be bridged. This also arouses concern on whether we can truly accomplish rational design of an efficient solid–solid interface, which requires simultaneous control over the solidification kinetics of not only one but two solids at both the atomic scale and the nanoscale. For instance, factors such as the contact tightness between particles, variations in work function, and the arrangement of atoms at the interface all impact the interface integrity. Hence, the controllable construction of heterogeneous interfaces also poses technical challenges. Developing methods to precisely regulate the composition and structure of solid–solid interfaces, particularly to achieve synergistic effects in actual electrode materials, is an area that still requires significant advancement.

Moving forward, overcoming these obstacles will require a concerted effort in interfacial engineering: the development of new advanced characterization techniques and innovative material design strategies. By addressing these limitations, researchers can unlock the full potential of solid–solid interfaces, further enhancing their role in advancing the efficiency and effectiveness of electrochemical catalytic systems.

## Author contributions

Wen-Xuan Liang: writing – original draft, formal analysis, and visualization; Huimin Han: writing – original draft, formal analysis, and visualization; Chun-Hua Zhen: project administration and supervision; Yingjie Hua: project administration and supervision; Jun-Tao Li: conceptualization, funding acquisition, and resources; and Yao Zhou: conceptualization, funding acquisition, resources, project administration, supervision, and writing – review and editing.

## Data availability

No primary research results, software or codes were included and no new data were generated or analysed as part of this review.

## Conflicts of interest

There are no conflicts to declare.

## Acknowledgements

The National Key Research and Development Program of China (no. 2022YFA1505300), the National Natural Science Foundation of China (no. 22072124, 22472142, 22288102), and the Natural Science Foundation of Fujian Province, China (no. 2024J09010) were acknowledged.

## Notes and references

- 1 Z. W. Seh, J. Kibsgaard, C. F. Dickens, I. Chorkendorff, J. K. Nørskov and T. F. Jaramillo, *Science*, 2017, **355**, eaad4998.
- 2 J. Kang, X. Yang, Q. Hu, Z. Cai, L.-M. Liu and L. Guo, *Chem. Rev.*, 2023, **123**, 8859–8941.
- 3 J. Wu and Y.-X. Yu, *Int. J. Hydrogen Energy*, 2023, **48**, 5961–5975.
- 4 J. Wu and Y.-X. Yu, *J. Phys. Chem. C*, 2022, **126**, 12460–12471.
- 5 T. X. Nguyen, Z.-Y. Wei, T.-M. Zheng, Y.-H. Su, K.-S. Chuang and J.-M. Ting, *Chem. Eng. J.*, 2024, **496**, 153841.
- 6 S. Samira, S. Deshpande, J. Greeley and E. Nikolla, *ACS Energy Lett.*, 2021, **6**, 665–674.
- 7 Q. Lu, X. Zou, Y. Bu and Z. Shao, *Energy Storage Mater.*, 2023, **55**, 166–192.
- 8 Y. Cheng and S. P. Jiang, *Prog. Nat. Sci.: Mater. Int.*, 2015, **25**, 545–553.
- 9 X. Long, J. Li, S. Xiao, K. Yan, Z. Wang, H. Chen and S. Yang, *Angew. Chem., Int. Ed.*, 2014, **53**, 7584–7588.
- 10 K. Wei, X. Wang and J. Ge, *Chem. Soc. Rev.*, 2024, **53**, 8903–8948.
- 11 J. Li, R. Güttinger, R. Moré, F. Song, W. Wan and G. R. Patzke, *Chem. Soc. Rev.*, 2017, **46**, 6124–6147.
- 12 W. Zhao, S. Yuan, L. Zhang, F. Jiang, Y. Yang, G. Zou, H. Hou, P. Ge, W. Sun and X. Ji, *Energy Storage Mater.*, 2022, **45**, 1183–1200.
- 13 X. Cheng, Y. Li, L. Zheng, Y. Yan, Y. Zhang, G. Chen, S. Sun and J. Zhang, *Energy Environ. Sci.*, 2017, **10**, 2450–2458.
- 14 T. Zhu, S. Liu, B. Huang, Q. Shao, M. Wang, F. Li, X. Tan, Y. Pi, S.-C. Weng, B. Huang, Z. Hu, J. Wu, Y. Qian and X. Huang, *Energy Environ. Sci.*, 2021, **14**, 3194–3202.
- 15 F. Luo, P. Yu, J. Xiang, J. Jiang and S. Chen, *J. Energy Chem.*, 2024, **94**, 508–516.
- 16 K. Ham, J. Lee, K. Lee and J. Lee, *J. Energy Chem.*, 2022, **71**, 580–587.
- 17 Z. J. Xu, *Nano-Micro Lett.*, 2017, **10**, 8.
- 18 P. Liu, A. Klyushin, P. Chandramathy Surendran, A. Fedorov, W. Xie, C. Zeng and X. Huang, *ACS Nano*, 2023, **17**, 24395–24403.
- 19 R. G. Rao, R. Blume, T. W. Hansen, E. Fuentes, K. Dreyer, S. Moldovan, O. Ersen, D. D. Hibbitts, Y. J. Chabal, R. Schlögl and J.-P. Tessonnier, *Nat. Commun.*, 2017, **8**, 340.
- 20 J. M. Kim, Y. J. Lee, S.-H. Kim, K.-H. Chae, K. R. Yoon, K. A. Lee, A. Byeon, Y. S. Kang, H.-Y. Park, M. K. Cho, H. C. Ham and J. Y. Kim, *Nano Energy*, 2019, **65**, 104008.
- 21 Y. Zhou, W. Yuan, M. Li, Z. Xie, X. Song, Y. Yang, J. Wang, L. Li, W. Ding, W.-F. Lin and Z. Wei, *Nat. Energy*, 2024, **9**, 1297–1309.
- 22 A. Wang, M. Du, J. Ni, D. Liu, Y. Pan, X. Liang, D. Liu, J. Ma, J. Wang and W. Wang, *Nat. Commun.*, 2023, **14**, 6733.
- 23 P.-F. Zhang, J.-H. Li, S.-J. Zhang, D.-C. Li, S.-Y. Zeng, S.-L. Xu, Q.-X. Yao, L.-Y. Liu, L. Ding, H.-X. Li, Y.-Y. Hu, J.-T. Li and Y. Zhou, *Adv. Funct. Mater.*, 2024, **34**, 2306359.
- 24 Q. Liang, J. Chen, Y. Zhou, J.-T. Li, L. Huang and S.-G. Sun, *Adv. Funct. Mater.*, 2021, **31**, 2104513.
- 25 Z. Tong, C. Lv, Y. Zhou, Z.-W. Yin, Z.-P. Wu and J.-T. Li, *Energy Storage Mater.*, 2024, **67**, 103301.
- 26 P.-F. Zhang, Y.-Y. Hu, X.-Y. Cui, J.-H. Li, S.-Y. Zeng, J. Li, H.-G. Hao, X.-J. Kong, Y. Zhou and J.-T. Li, *Mater. Today Phys.*, 2024, **40**, 101307.
- 27 H. Wang, L. Xu, Y. Bai and Z. L. Wang, *Nat. Commun.*, 2020, **11**, 4203.
- 28 K. Mustonen, A. Hussain, C. Hofer, M. R. A. Monazam, R. Mirzayev, K. Elibol, P. Laiho, C. Mangler, H. Jiang, T. Susi, E. I. Kauppinen, J. Kotakoski and J. C. Meyer, *ACS Nano*, 2018, **12**, 8512–8519.
- 29 X. Su, K. Guo, T. Ma, P. A. Tamirisa, H. Ye, H. Gao and B. W. Sheldon, *ACS Energy Lett.*, 2017, **2**, 1729–1733.
- 30 Y. Zhou and H. C. Zeng, *J. Phys. Chem. C*, 2016, **120**, 29348–29357.
- 31 J. Zhang, J.-J. Dai, D.-Q. Cao, H. Xu, X.-Y. Ding, C.-H. Zhen, B. Paulus, J.-Y. Ye, Q. Liang, J.-K. Liu, S.-J. Xie, S.-S. Deng, Z. Wang, J.-T. Li, Y. Zhou and S.-G. Sun, *J. Energy Chem.*, 2023, **83**, 313–323.
- 32 P.-F. Zhang, J.-Y. Zhang, T. Sheng, Y.-Q. Lu, Z.-W. Yin, Y.-Y. Li, X.-X. Peng, Y. Zhou, J.-T. Li, Y.-J. Wu, J.-X. Lin, B.-B. Xu, X.-M. Qu, L. Huang and S.-G. Sun, *ACS Catal.*, 2020, **10**, 1640–1651.
- 33 P.-F. Zhang, T. Sheng, Y. Zhou, Y.-J. Wu, C.-C. Xiang, J.-X. Lin, Y.-Y. Li, J.-T. Li, L. Huang and S.-G. Sun, *Chem. Eng. J.*, 2022, **448**, 137541.
- 34 P.-F. Zhang, Y.-Q. Lu, Y.-J. Wu, Z.-W. Yin, J.-T. Li, Y. Zhou, Y.-H. Hong, Y.-Y. Li, L. Huang and S.-G. Sun, *Chem. Eng. J.*, 2019, **363**, 224–233.
- 35 Z. Wang, L. Deng, X.-R. Yang, J.-X. Lin, D.-Q. Cao, J.-K. Liu, Z. Tong, J. Zhang, G.-Y. Bai, Y.-X. Luo, Z.-W. Yin, Y. Zhou and J.-T. Li, *Adv. Funct. Mater.*, 2024, **34**, 2404137.
- 36 D. N. Basov, M. M. Fogler and F. J. García de Abajo, *Science*, 2016, **354**, aag1992.
- 37 Y. Liu, Y. Huang and X. Duan, *Nature*, 2019, **567**, 323–333.
- 38 H. Xu, S.-J. Xie, C. Lv, J.-T. Li, Y. Zhou and S.-G. Sun, *J. Mater. Chem. A*, 2023, **11**, 10277–10286.
- 39 K. Carter-Fenk and J. M. Herbert, *Phys. Chem. Chem. Phys.*, 2020, **22**, 24870–24886.
- 40 W. Hao, B. Guo, J. Liu, Q. Ren, S. Li, Q. Li, K. Zhou, L. Liu and H.-C. Wu, *J. Am. Chem. Soc.*, 2024, **146**, 10206–10216.
- 41 Z. Liu, T. Lu and Q. Chen, *Carbon*, 2021, **171**, 514–523.
- 42 Y. Chen, J. Ma, Q. Peng, X. Gong, J. Lin, X. Qi and H. Guo, *ACS Appl. Mater. Interfaces*, 2022, **14**, 20896–20906.
- 43 L. Pauling, *J. Am. Chem. Soc.*, 1935, **57**, 2680–2684.
- 44 M. Ekimova, C. Kleine, J. Ludwig, M. Ochmann, T. E. G. Agrenius, E. Kozari, D. Pines, E. Pines, N. Huse, P. Wernet, M. Odellius and E. T. J. Nibbering, *Angew. Chem., Int. Ed.*, 2022, **61**, e202211066.
- 45 C. Guhl, J. Rohrer, P. Kehne, T. Ferber, L. Alff, K. Albe, W. Jaegermann, P. Komissinskiy and R. Hausbrand, *Energy Storage Mater.*, 2021, **37**, 190–198.
- 46 J. Chen, F. Zheng, S.-J. Zhang, A. Fisher, Y. Zhou, Z. Wang, Y. Li, B.-B. Xu, J.-T. Li and S.-G. Sun, *ACS Catal.*, 2018, **8**, 11342–11351.
- 47 Y.-J. Wu, J. Yang, T.-X. Tu, W.-Q. Li, P.-F. Zhang, Y. Zhou, J.-F. Li, J.-T. Li and S.-G. Sun, *Angew. Chem., Int. Ed.*, 2021, **60**, 26829–26836.
- 48 Y. Zhou and H. C. Zeng, *ACS Sustainable Chem. Eng.*, 2019, **7**, 5953–5962.
- 49 C. Wagner, *J. Phys. Chem. Solids*, 1972, **33**, 1051–1059.
- 50 Z. Zhang and J. T. Yates, Jr., *Chem. Rev.*, 2012, **112**, 5520–5551.
- 51 S. Jia, H. Han, B. Wang, J. Liu, Q. Tang, G. Liu, Q. Ruan, X. Zhu, H. Li, C. Wang, P. K. Chu and Y. Hua, *Appl. Catal., B*, 2024, **353**, 124050.
- 52 S. Sun, R. Gao, X. Liu, L. Pan, C. Shi, Z. Jiang, X. Zhang and J.-J. Zou, *Sci. Bull.*, 2022, **67**, 389–397.
- 53 W. Li, C. Liu, C. Gu, J.-H. Choi, S. Wang and J. Jiang, *J. Am. Chem. Soc.*, 2023, **145**, 4774–4783.
- 54 B. Wang, H. Chen, W. Zhang, H. Liu, Z. Zheng, F. Huang, J. Liu, G. Liu, X. Yan, Y.-X. Weng, H. Li, Y. She, P. K. Chu and J. Xia, *Adv. Mater.*, 2024, **36**, 2312676.
- 55 Y.-J. Wu, X.-H. Wu, T.-X. Tu, P.-F. Zhang, J.-T. Li, Y. Zhou, L. Huang and S.-G. Sun, *Appl. Catal., B*, 2020, **278**, 119259.
- 56 L. Yu, D. Deng and X. Bao, *Angew. Chem., Int. Ed.*, 2020, **59**, 15294–15297.
- 57 Y. Song, X. Yang, H. Liu, S. Liang, Y. Cai, W. Yang, K. Zhu, L. Yu, X. Cui and D. Deng, *J. Am. Chem. Soc.*, 2024, **146**, 5834–5842.
- 58 Q. Liang, Y. Zhao, J.-D. Chen, J.-J. Dai, X. Ding, Z. Tong, S.-J. Xie, J. Zhang, Z.-H. Zhou, J.-T. Li, J.-F. Li and Y. Zhou, *Chem. Mater.*, 2022, **34**, 5607–5620.
- 59 H.-W. Chen, D.-Q. Cao, S.-J. Xie, J.-J. Dai, Z.-H. Dai, C.-H. Zhen, J.-F. Li, B. Paulus, Z.-W. Yin, J.-T. Li, Y. Zhou and S.-G. Sun, *Angew. Chem., Int. Ed.*, 2024, **63**, e202317922.